3D structure modeling of dense capillaries by multi-objects tracking

Ryoma Bise, Imari Sato
National Institute of Informatics, Japan
{bise-r, imarik}@nii.ac.jp

Kentaro Kajiya, Toyonobu Yamashita
Shiseido Global Innovation Center, Japan
kentaro.kajiya@to.shiseido.co.jp
toyonobu.yamashita@to.shiseido.co.jp

Abstract

A newly developed imaging technique called light-sheet laser microscopy imaging can visualize the detailed 3D structures of capillaries. Capillaries form complicated network structures in the obtained data, and this makes it difficult to model vessel structures by existing methods that implicitly assume simple tree structures for blood vessels. To cope with such dense capillaries with network structures, we propose to track the flow of blood vessels along a base-axis using a multiple-object tracking framework. We first track multiple blood vessels in cross-sectional images along a single axis to make the trajectories of blood vessels, and then connect these blood vessels to reveal their entire structures. This framework is efficient to track densely distributed vessels since it uses only a single cross-sectional plane. The network structure is then generated in the post-processing by connecting blood vessels on the basis of orientations of the trajectories. The results of experiments using a challenging real data-set demonstrate the efficacy of the proposed method, which are capable of modeling dense capillaries.

1. Introduction

It is known that vascular structures are related many diseases, *i.e.,* cancer, malignancy of brain tumor, and analyzing vascular structure is important in medical biomedical studies. MRI and CT, which can visualize arteries and veins, have been widely used for such clinical practice, and many automatic methods have been developed for segmenting and modeling blood vessels in MRI and CT, in order to identify and quantitate morphological abnormalities of vessels.

Recently, in addition to such modalities, novel imaging techniques, *i.e.*, photoacoustic imaging and light-sheet microscopy imaging, have been developed to visualize and analyze more detailed structures of blood vessels. For example, a light-sheet microscope, which obtains multi-layer projections inside a transparent tissue [11], is capable of visualizing the detailed structures of capillaries on the surface of skins, where this technique is promising for research and development in biology and medicine. Figure 1 shows examples of maximum intensity projection (MIP) of a microscopic image at facial capillaries. In this figure, we see that the blood vessels are densely located and makes dense networks.

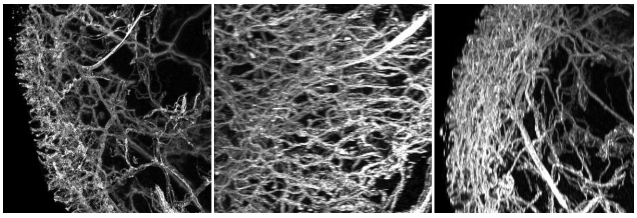

Figure 1. Examples of maximum intensity projection (MIP) obtained from a sheet-laser microscope. Left: x-y, Middle: y-z, Right: z-x.

The main difficulties arise from two aspects of the problem in modeling such dense capillaries. First, contrast to arteries and veins that usually have tree structures from the heart to arterioles or from venula to the heart, capillaries make dense network structures in the surface of skins. Existing blood vessel modeling methods that track a single vessel independently have limitations to track these dense capillaries, since these methods basically require initialization of the root position to decide the starting position of tracking. Second, the number of capillary blood vessels is much larger than those of blood vessels visualized by MRI and CT. Existing individual vessel tracking approaches that search cross-sectional plane for each searching point of each vessel curve, are not efficient for tracking such many vessels.

To model the 3D structures of such dense capillaries for identifying single vessel curves, and their connection, we propose a multiple-object tracking based modeling method. The method first tracks multiple blood vessels in cross-sectional images along a single axis to make the vessel curves as shown in Figure 2(a), and then connects these blood vessels (Figures 2(b),(c)). In order to reliably track multiple cross-sectional blood vessel regions while vessels are closely located, we modify a cell tracking method in microscopic images [2] that simultaneously solves the joint

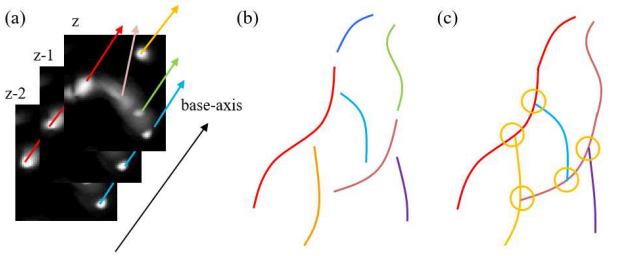

Figure 2. (a)Illustration of tracking cross-sectional blood vessel regions along a base-axis. (b) Illustration of generated vessel curves, (c) vessel network structures obtained by connecting vessel curves from (b), where each color indicates each vessel curve, and the orange circle indicates the bifurcation.

problem of segmentation and association between successive frames. This makes it possible to make more reliable vessel curves under high density conditions compared with typical detection-and-association methods. In addition, we newly introduce a connecting method that connects blood vessels on the basis of orientation of the vessel curves and the intensities of the original data to identify the network structures. This framework efficiently track such many vessels since it uses only a single cross-sectional plane for tracking multiple vessels at once, comparing with the existing methods that track a single vessel curve. The results of experiments using a challenging real data-set demonstrate the efficacy of the proposed method, which are capable of modeling dense capillaries.

2. Related works

Vascular segmentation and modeling methods have been intensively studied in 3D volume in MRI and CT, these are well overviewed in [7], [8]. Vascular structure modeling methods can be roughly classified into two groups: the segmentation-and-modeling group, and tracking-based group.

The first group segments vascular regions on the basis of intensity distributions around each pixel, and model each blood vessel as the center line of segmented regions and their bifurcations. The simple segmentation algorithms were developed based on thresholding and region growing [1], [16]. Since the segmentation largely depends on image intensities, neighboring non-vessel tissue is sometimes misclassified as blood vessels when the contrast of an original image is low. For more robust segmentation, vessels are extracted as tubular structure in a pre-processing step by examining the eigenvectors of the Hessian matrix of a local area, to compute the likeliness of tubular structure [4], [9]. More recently, energy minimizing deformable models, *i.e.*, level-set, have been applied to define contours of the vessel surfaces [15],[18],[5]. These pixel-driven segmentation techniques, however, do not take the shapes of brood vessels into consideration and are thus largely affected by noise.

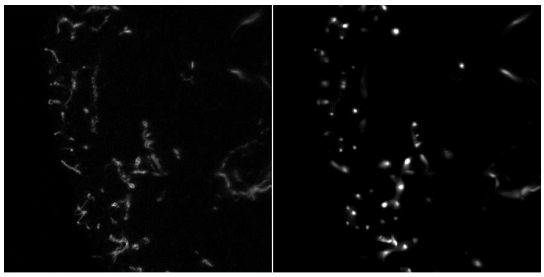

Figure 3. Examples of a z-slice obtained from a sheet-laser microscope. Left: original image, Right: Frangi-filter response.

Even when they succeed in segmenting the blood vessel regions, the complicated modeling procedures as identifying the center-lines of each blood vessel and their connection are further required for revealing the vascular structures.

The second group of vascular modeling methods tracks each blood vessel, where these methods identify the center line of each vessel during the segmentation. This group can be sub-classified into ridge tracking, tubular tracking, and cross-section tracking, that are well reviewed in [6]. Ridge tracking methods track vessels as intensity ridges using gradient information [17] or second-order information in the Hessian matrix [10]. Tubular tracking approaches track vessels with modeling a local area of a vessel as a linear tube segment using cylindroidal superellipsoid [14] and 3D template matching [6]. The cross-section tracking methods fit a 2D structure model, such as ellipse, into the 2D cross-sectional vessel region while identifying the cross-sectional plane based on the orientation of the vessel [3],[12]. These methods basically track a single vessel independently and require initialization of a root position, where the methods implicitly assume that vascular structures are tree structures, not as network: the vessel curves flows from a root to branches in one direction.

The sheet-laser microscope can provide much richer information on capillary blood vessels that often make complicated networks. This requires the initialization process for identifying endpoints of each vessel for the current cross-sectional tracking methods. In addition, the number of capillary blood vessels is much larger than those of blood vessels in MRI and CT. The individual vessel tracking approaches that search cross-sectional plane for each searching point of each vessel curve, are not efficient for tracking such many vessels. Our method tracks many blood vessels along a single base-axis at once and connects the vessels: This is efficient to tracks many blood vessels comparing with the existing methods.

3. Method

In this paper, we propose a multiple-object tracking based modeling method that can reveal the details structures of dense capillaries. The proposed method first enhances

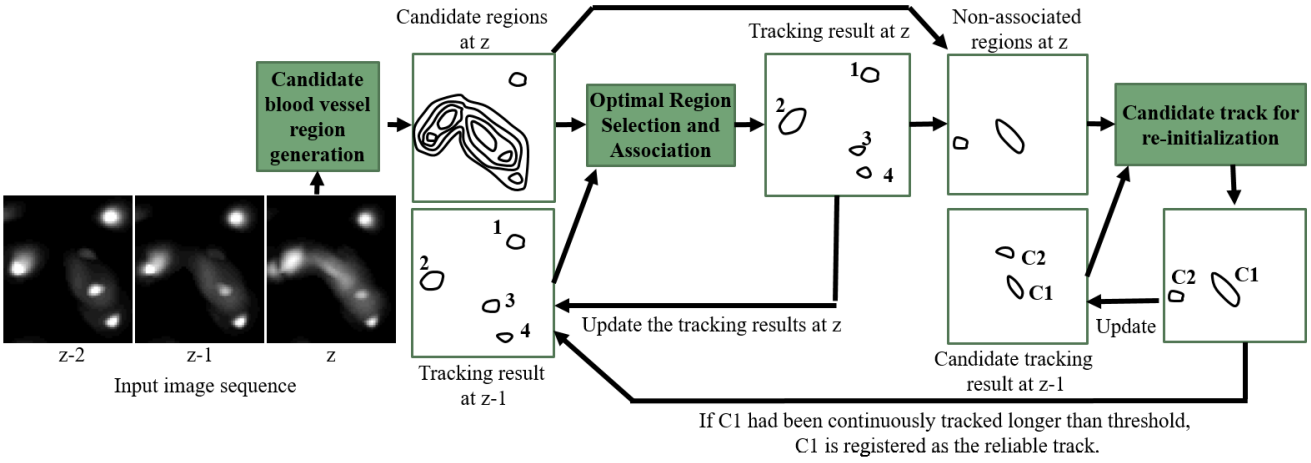

Figure 4. Overview flow of blood vessel curve generation.

the blood vessel regions using the multi-scale Frangi-filter [4]. Next, the method models vessel structures by tracking blood vessels detected in each slice of base-axis, Then, the method models the network structure by connecting blood vessels on the basis of orientations of the vessel curve. The details of this procedure are described in the following sections.

3.1. Blood vessel enhancement

The multi-scale Frangi-filter [4] is applied to the 3D volume to reduce the noise and enhance blood vessels. The multi-scale Frangi-filter method computes the likeliness of tubular structure on the basis of the eigenvectors of the Hessian matrix for multiple scale Gaussian filters, then combines their responses. We briefly explain the filtering method below. The axes are first scaled up using linear spline interpolation to provide isotropic voxels as required in the multi-scale Frangi-filter method. The 3D volume data $L(x)$ is convolved with a three-dimensional isotropic derivative of a Gaussian filter $G(x, \sigma)$ for each local area around pixel x, where the standard deviation σ indicates the scale of the tubes. Then, the likeliness of tubular structure at each voxel is computed based on the eigenvalues of the second derivative of a Gaussian kernel (Hessian) at each σ as:

$$\nu_o(x,\sigma) = \begin{cases} 0, \text{ if } \lambda_2 > 0 \text{ or } \lambda_3 > 0 \\ (1 - e^{\frac{-\lambda_2^2}{2\alpha^2\lambda_3^2}}) e^{\frac{-\lambda_1^2}{2\beta^2\|\lambda_2\lambda_3\|}} (1 - e^{\frac{-\sum_i \lambda_1^2}{2c^2}}) \end{cases} \quad (1)$$

where λ_1, λ_2, and λ_3 ($|\lambda_1| \leq |\lambda_2| \leq |\lambda_3|$) are the eigenvalues of $H_o(x, \sigma)$, and $\boldsymbol{v}_1(x, \sigma)$, $\boldsymbol{v}_2(x, \sigma)$ and $\boldsymbol{v}_3(x, \sigma)$ are corresponding eigenvectors respectively. The first term is a measure between plate-like and line-like structures, the second term is a measure of how similar the local structure is to a blob, and the third term is a measure of the contrast. α and β are the relative weight of these terms. The responses of multiple scales are combined by selecting the maximum response:

$$\nu_o(x) = max_{\sigma \in \{\sigma_0 \ldots, \sigma_S\}} \nu_o(\sigma) \quad (2)$$

where S is the number of the scale. The corresponding eigenvectors of the selected σ are $\boldsymbol{V}_1(x)$, $\boldsymbol{V}_2(x)$, and $\boldsymbol{V}_3(x)$.

The left image in Figure 3 shows a z-slice obtained from a light-sheet microscope, where it is difficult to distinguish the regions of the closely located blood vessels. The right image in Figure 3 shows a z-slice of the multi-scale Frangi-filter response data. In this result, a region of a single blood vessel is clearer than that in the original image. We use this vessel-enhanced data in the following steps.

3.2. Blood vessel curve generation

The response values from Frangi-filter at the bifurcation points are usually not high since a local structure of such points has a plane-like structure. In this step, we track cross-sectional regions of each blood vessels along a single axis to generate vessel curve, without considering connections of them.

We define the base-axis for tracking on the basis of the primary direction of vessels. We first segment the blood vessel regions by Otsu-thresholding[1]. Then, we define a base-axis using the principal component analysis (PCA) of the set of eigenvectors $\boldsymbol{V}_1(x)$ in the segmented regions, which is the smallest eigenvalue at each voxel x, and this corresponds to the direction of vessels in the local area around x [9]. We set the first component vector as the base-axis, and transform the image using the base-axis. Hence, the base-axis is called as z axis, and the others are x and y axes in this paper.

[1]This region is only used for computing the direction of vessels and not used for the segmentation and modeling. Therefore, the rough segmentation is enough in this step

To model the vessel curves, we track the multiple cross-sectional regions of vessels along the base-axis, which is on the basis of the fact that the cross-sectional regions of vessel regions appear ellipse-like shape in each z-slice and the fact that the cross-sectional regions in successive slices of the same vessels are nearly located as shown in Figure 4. The ambiguity parts, *i.e.,* very low intensity part and bifurcation points, are connected in the next step after generating vessel curves.

Since this cross-sectional region tracking problem is similar with a cell tracking problem that tracks multiple cell regions along the temporal image sequence, we follow a cell tracking method for dense cell conditions [2] to track vessel regions, which uses the cell region information from the previous frame to help segment the blurry regions, rather than relying on only the image appearance at the current frame. To fit the method to the vessel modeling problem, we modify several sub-processes: the candidate region tree pruning, the association score computing and re-initializing process.

The overview of the vessel curve generation method is shown in Figure 4. We first detects candidate regions of blood vessels, so that they include false positives but in turn very few false negatives. Next, the joint problem of selecting optimal regions and associating between the candidate regions at the current slice and the tracking results from the previous slice is simultaneously solved. In this example in Figure 4, four regions are selected as blood vessels. Then, to identify newly appeared blood vessels, the re-initialization step tracks non-associated regions at z, that are not conflicted with the selected vessel regions, as a candidate track. This step starts the tracking process for a candidate region only if the boundary of the candidate has been clear for several frames continuously, and removes the other candidate tracks as noise. This process is iteratively performed for each z-slice until the end of the sequence to make vessel curves. The blood vessel generation process is described in more detail below.

3.2.1 Candidate region and tree generation

In this step, a set of candidate regions are produced so that they include many false positives but in turn very few false negatives. The method is based on the fact that cross-sectional regions of blood vessels appear bright under Frangi-filter response and on the fact that the intensities on the inside of a vessel are slightly higher than those at its boundaries among touching blood vessels. Candidate regions are identified by segmenting all regions by using multiple-level thresholding as shown in Figure 5(a). We set K level thresholds (we set K as 50 in all our experiments), that are equally spaced, and each threshold is used to segment images at a particular level of intensity. The holes of the foreground region are filled since a blood vessel does not have holes.

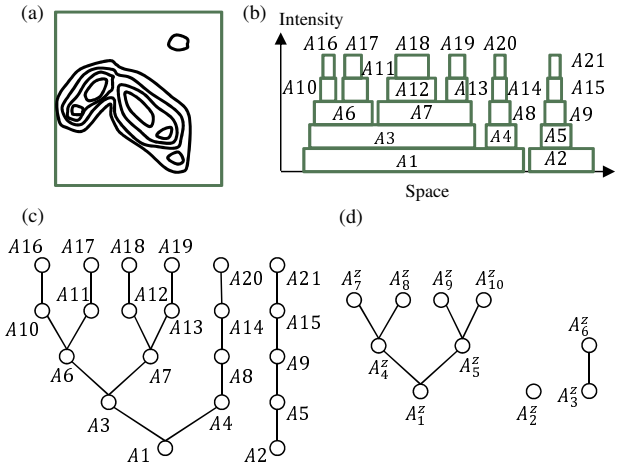

Figure 5. Illustration of candidate blood vessel region generation process. (a) Example illustration of detected candidates corresponding with the input image at z in Figure 4. (b) Illustration of the relationships of the regions and the intensity level. (c) Original tree that describes containment relationships among candidate regions obtained from (b). (d) Pruned tree.

The detected blood vessel candidates constitute a tree structure which describes containment relationships of those regions (Figure 5), where a candidate region A_j is a child node of A_i, if A_j is inside A_i.

To reduce computational costs, we prune some nodes of the tree. We prune the nodes on the basis of two concepts. First, this step prunes large and small candidate regions that does not match the expected cross-sectional region size of blood vessels using the size range $[\theta_{min}, \theta_{max}]$, where a candidate region that size is out-of-range is eliminated. Second, we prune the similar structure and similar shape regions, which have no brother node, and the size of the region closes enough to the size of it's parent node. For example in Figure 5(c), $A9$ is pruned since $A5$ has only one child node $A9$. Since the size ratio between $A5$ and it's parent node $A2$ is less than a threshold τ_s, $A5$ is not pruned though $A5$ have no brother node. Finally, the pruned tree nodes are registered as candidate blood vessel regions. A set of candidate regions is denoted as $\mathbf{A^z} = \{A_i^z, i = 1, 2, ..., N_z\}$, where A_i^z represents the i-th candidate vessel region, and N_z is the number of candidate regions.

The tree structure is used to handle non-overlapping constraints for solving joint problem of selecting optimal regions from candidates and associating blood vessel regions successive slices.

3.2.2 Optimal region selection and association

After generating the candidate blood vessel regions and the tree structure, we simultaneously solve the problem of selecting optimal regions and association problem between candidate regions in the current slice z and tracked blood vessel regions that have been tracked up to slice $z-1$. This problem is solved by a binary linear programming problem with containing constraints to avoid conflict associations, in which overlapped regions are not concurrently selected in the optimal solution.

All possible blood vessel connection hypothesis $\mathbf{H}_z$ at each successive slices are first listed. If the overlap ratio between the tracked region T_i^{z-1} and the candidate region A_j^z is larger than a threshold τ_o, a connecting hypothesis $h_l^z = \{T_i^{z-1} \rightarrow A_j^z\}$ is added to the hypothesis set $\mathbf{H}_z = \{h_k^z, k = 1, 2, ..., H_z\}$, where H_z is the number of hypotheses in slice z.

After listing up the hypothesis, the method selects the optimal hypothesis set for region selection and association from all hypotheses $\mathbf{H}_z$ with avoiding two types of hypotheses conflict. First, a tracked blood vessel region is associated to only one candidate region (i.e., one-to-one matching is allowed in this step). Second, any selected regions in the solution do not overlap their regions. This problem is formulated as a binary linear programing problem for maximizing the sum of the scores of the hypotheses under non-overlapping constraints.

Let N_1 be the number of tracked blood vessel regions at the slice $z-1$, let N_2 be the number of candidate regions at the slice z, let vector $\boldsymbol{\rho}$ store the scores of every possible hypothesis, and let matrix C store the constraints to avoid conflict hypotheses, where each row of C has N_1+N_2 columns and each column on 1 to N_1 indicates tracked vessel index and each column on N_1+1 to N_1+N_2 indicates candidate region index on the association between track results and candidate regions. $\Omega(A_i^z)$ is a set of candidate region indexes that are all descendant node indexes of A_i^z in the tree, where the set includes itself A_i^z. For example, in Figure 5(d), $\Omega(A_1^z)$ is $\{1, 4, 5, 7, 8, 9, 10\}$ since the candidate region A_1^z is overlapped with all of the other candidates. Let h be the index of a hypothesis $h_h^z = \{T_l^{z-1} \rightarrow A_m^z\}$, where h-th row of C and a corresponding score of $\boldsymbol{\rho}$ are determined as:

$$C(h,i) = \begin{cases} 1, & \text{if } i = l \text{ or } i = N_1 + m_r, m_r \in \Omega(A_m^t) \\ 0, & \text{otherwise.} \end{cases} \quad (3)$$

$$\boldsymbol{\rho}(h) = P_{con}(A_m^z | T_l^{z-1}) P_{TP}(A_m^z), \quad (4)$$

where $P_{con}(A_m^t | T_l^{z-1})$ is the score of the connecting hypothesis $\{T_l^{z-1} \rightarrow A_m^z\}$. $P_{TP}(A_m^z)$ is the score in which the region of A_m^z is a single vessel region. For implementation, when the interval of z-slice is short enough, we use 'relative overlap' between tracked vessel region T_l^{z-1} and candidate region A_m^z, *i.e.*, $P_{con}(A_m^z | T_l^{z-1}) = \frac{T_l^{z-1} \cap A_m^t}{T_l^{z-1} \cup A_m^t}$.

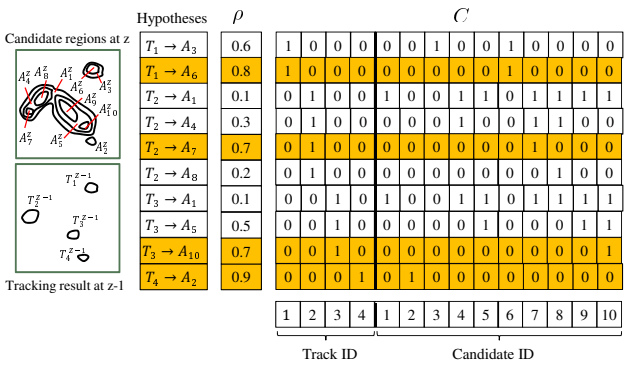

Figure 6. Example of a constraint matrix and score vector for jointly solving detection and association, where the z-slice index is omitted.

For the score of vesselness of the candidate region, we assume that a cross-sectional region of vessel has a circular shape since a blood vessel shape has tube structure. For the implementation, we compute the circularity for the score in which the candidate region A_m^z is a single blood vessel region as:

$$P_{TP}(A_m^z) = \frac{4 \times \pi \times S(A_m^z)}{B(A_m^z)} \quad (5)$$

where $S(A_m^z)$ is the size of the region A_m^z (the number of pixels), and $B(A_m^z)$ is the length of boundary of the region. After computing the score vector $\boldsymbol{\rho}$ and constraint matrix C of all H hypotheses over N_1 tracked blood vessels and N_2 candidate regions, the association problem can be formulated as the following binary linear programming:

$$\boldsymbol{x}^* = \arg\max_{\boldsymbol{x}} \boldsymbol{\rho}^T \boldsymbol{x}, \quad s.t. \;\; C^T \boldsymbol{x} \leq \mathbf{1}, \quad (6)$$

where $\boldsymbol{x}$ is a $H \times 1$ binary vector and $x_k = 1$ means the kth hypothesis is selected in an optimal solution. To solve this problem, we use the branch-and-bound algorithm which divides the original problem into all possible sub-problems, and solves a series of LP-relaxation problems in each sub-problem. The constraint $C^T \boldsymbol{x} \leq \mathbf{1}$ guarantees that conflict hypotheses are not included in the solution at once.

Figure 6 shows a simple example of a binary linear programming problem in which the number of tracking results at the previous frame is 4 and the number of candidate regions is 10. In the hypothesis $T_{z-1}^2 \rightarrow A_1^z$, the set of descendant candidates with A_1^z is $\{1, 4, 5, 7, 8, 9, 10\}$. This constraint indicates that the candidates $\{4, 5, 7, 8, 9, 10\}$ are not associated with any tracked vessels if the region A_1^z is selected as an optimal solution. In this example, the hypotheses $T_1^{z-1} \rightarrow A_6^z$, $T_2^{z-1} \rightarrow A_7^z$, $T_3^{z-1} \rightarrow A_{10}^z$ and $T_4^{z-1} \rightarrow A_6^z$ are selected as the optimal solution. Based on this process, a set of vessel curves $\mathbf{X} = \{X_i\}$ is generated.

The term $X_i = \{R_{i_j}\}$ is a vessel curve consisting of an order list of associated cross-sectional vessel regions where the associated candidate region is registered as R_{i_j}, which indicates the jth detection result on vessel curve X_i.

3.2.3 Candidate tracking for re-initialization

Blood vessels that connect from upper z-slice suddenly appear in tracking process along z-slice, since the tracking process usually track vessel regions from bottom to upper slices. In addition, a boundary of a blood vessel is sometimes clear and sometimes blurry: this results in failing to track such blurry vessels even though the candidate region detection step produces redundant regions. Therefore, re-initialization is required for re-tracking such vessels.

All candidate regions in z-slice that are not associated with any tracked blood vessels have possibility to be newly appeared regions. However, these candidates include many false-positives as discussed above. To determine which candidate regions be registered as new vessels in the set of candidate regions and which are not tracked, we only initialize regions and starts the tracking process if the boundary of the vessel region has been clear for several slices continuously.

The method first removes conflict candidates that are overlapped with selected optimal blood vessel regions in the process described in Section 3.2.2 at each slice $z-1$ and z. Here, the rest of the candidate regions is denoted as $\mathbf{A2^z} = \{A2_i^z\}$. Next, the method determines which regions have boundaries that are continuously clear in several consecutive slices, as these are considered reliable. The candidates $\mathbf{A2^z}$ and the candidate track regions $\mathbf{T2^{z-1}}$, that have been tracked up to slice $z-1$ as candidate tracks, are associated by using the similar method proposed in section 3.2.2, where the only difference is the association score $\boldsymbol{\rho}(h)$ of the hypothesis $T2_l^{z-1} \rightarrow A2_m^z$.

$$\boldsymbol{\rho}(h) = P_{con}(A2_m^z | T2_l^{z-1}) P_{TP}(A2_m^z) P_{TP}(T2_l^{z-1}) \quad (7)$$

$$P_{TP}(A2_m^z) = e^{-\frac{1}{E_{edge}}\frac{1}{\sigma}} \quad (8)$$

$$E_{edge}(A_m^z) = \frac{1}{length(\Phi_{A_m^z})} \int_{\Phi_{A_m^z}} e(\Phi_{A_m^z}) dl, \quad (9)$$

where the edge energy E_{edge} measures the edgeness along the region boundaries. $\Phi_{A2_m^z}$ is the region boundary of candidate region $A2_m^z$. The function $e(\cdot)$ is the edgeness metric, which takes a large value if the intensity gradient on $\Phi_{A2_m^z}$ is large. $length(\Phi_{A2_m^z})$ indicates the length of the region boundary. When the edgeness of the region boundary takes a larger value, the score $P_{TP}(A2_m^z)$ closes to 1.

Using this score, the optimal candidate regions and associations are solved by linear programming. Here, the high value of the score indicates that both boundaries of the regions $A2_m^z$ and $T2_l^{z-1}$ are clear and that these regions appear to be the same object. The purpose of this step is to initialize the tracker for clear blood vessel regions. Thus, the associated candidate region is linked to a candidate track if and only if its score is higher than a threshold. These selected regions are tracked until the reliability of the association is less than threshold. Then, if the length of the generated candidate track is longer than a threshold (default is 5), the vessel curve is registered as reliable. Non-associated regions in this step are newly added to the candidate track $\mathbf{T2^z}$, if the non-associated region is not conflict with the selected candidate track regions at z.

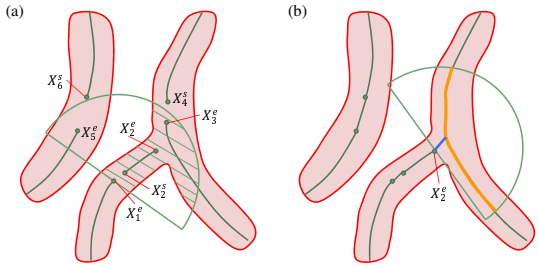

Figure 7. Example illustration of the process of connecting vessel curves. (a) Example of the process of connecting endpoints. (b) Example of the process of connecting the endpoint and branch point. The red regions are the intensity-based search area, and the green half sphere area is the vessel curve direction and distance based search area. The shaded area with green diagonal lines is final search area.

3.3. Vessel curve connection

After generating blood vessel curves, we connect them by two steps. First we connect endpoints of blood vessels that are disconnected in tracking step. Second, we also connect a endpoint and a middle point of vessel curves, which indicates the bifurcation point. In these connecting process, we only use sequence of centroid points of each region for vessel curve, instead of regions, and we denote endpoints of a vessel curve X_i as X_i^s and X_i^e, where X_i^s is the endpoint on the lower z-slice, and X_i^e is that on the higher slice.

To connect endpoints, we first list up connecting hypotheses, in which two endpoints are in a search area. If the search area is decided on the basis of only the distance from the endpoint, it results in producing improbable connecting hypotheses, in which the connected interpolate vessel curves between two endpoints passes zero-value voxels. To reduce such problem, we introduce the intensity-based search area, which relies on the fact that the intensities of blood vessel curves are slightly higher than the background in original data, where we use the original data instead of the filtered data, since Frangi-filter sometimes responses a very low value when the local structure is not tubular-like even though the region have some intensities. The intensity-based area is segmented by a lower thresholding that is r times the result of Otsu-thresholding of original volume (we set r as 0.7 on the all of experiments). In addition, we introduce another search area which is decided by the direc-

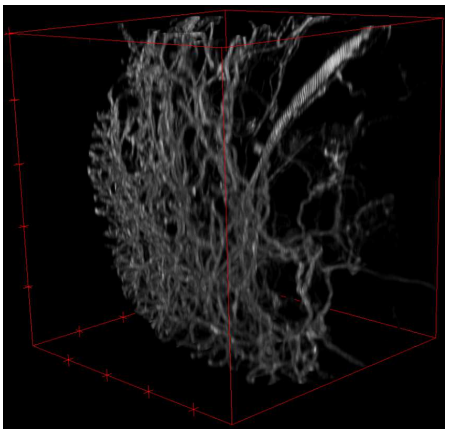

Figure 8. Example of volume rendering of the original volume on the surface of facial skins.

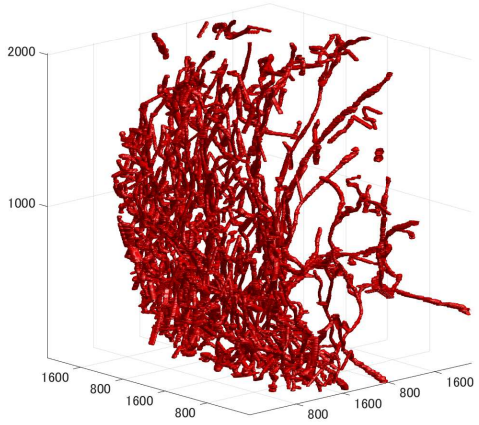

Figure 9. Example of volume rendering of the segmented blood vessel regions from the proposed method.

tion of the vessel curves and the distance from the endpoint, where the direction vector is simply decided by the neighbor points of the endpoint, and the distance is decided by thresholding γ_d. The connected intersectional area of these areas is the final search area to find connecting hypotheses, where unconnected intersectional area is not in search area. Figure 7(a) shows an example of search area for endpoint X_1^e. In this example, three hypotheses $\{X_1^e \rightarrow X_2^s\}$, $\{X_1^e \rightarrow X_2^e\}$, and $\{X_1^e \rightarrow X_3^e\}$ are registered in the set of connecting hypotheses.

After listing up connecting hypotheses, we select optimal connections from the set of the all hypotheses. For each hypothesis, we first interpolate the vessel curve between the endpoints by linear interpolation, then compute the hypothesis score calculated as $-\Sigma_x\{1 - I(x)\}$, where I is the intensity sequence of interpolated vessel curve, x is a point of I. The score takes a small value if the intensities on the interpolated vessel curve are small and the length of the interpolated curve is long. After computing the hypothesis scores, the optimal set of hypotheses is selected by minimizing the sum of the hypothesis scores with one-to-one matching constraint in similar fashion with the method discussed on the previous section. The identification of the connected vessel curves is re-labeled and registered in the set of vessel curves $\mathbf{X}$.

Next, we identifies bifurcation points by connecting an endpoint and a middle point of a vessel curve. To find this, we also use the same search area as above. The endpoint is connected to a vessel curve when a part of the vessel curve is in the search area. To decide the bifurcation point, we compute all of scores in the same as above which use intensities and select the minimum one as the bifurcation point. Figure 7(b) shows the example of this step, where the orange curve is the candidate points of the bifurcation, and blue line is selected interpolated line.

4. Experimental results

The proposed method was applied to the real data of capillarities on the surface of facial skins. To observe inside skins, the skins were transparent using an effective tissue-clearing technique [13], and the blood vessels were stained using fluorescent protein. Then, a z-slice of the stained capillarities in the skin was captured at a resolution of 1920×1920 pixels per image with a digital scanned light-sheet microscope (DSLM). The number of z-slice was 324, and the voxel size of each axis was $[0.834, 0.834, 5.085]\mu m$. The z-stack images were treated as 3D volume data, where one pixel in a z-stack image was treated as a voxel in 3D. To make the voxel size isotropic, the z-axis was scaled up using linear spline interpolation. Example of the volume rendering is shown in Figure 8.

For quantitative evaluation, we manually annotated the centerlines of blood vessels[2]. Since it is extremely time-consuming to annotate all blood vessels in the entire data, all vessels in a box $800 \times 800 \times 800$ were annotated. The total number of vessels were 141, and the total number of annotating points were 3476. The manual tracking results were used for computing the recall ($\frac{TP}{TP+FN}$), precision ($\frac{TP}{TP+FP}$) and F-measure ($2 \cdot \frac{precision \cdot recall}{precision+recall}$) for blood vessel detection accuracies, where TP is the number of true positives, FP is the number of false positives, FN is the number of false negatives, and F-measure is the harmonic mean of precision and recall.

Figure 9 shows the example of the segmentation results which corresponded with Figure 8. In this results, the main structures of vessels were well modeled. Since the blood vessels were too dense, it is difficult to compare the segmentation results and original data in detail. Therefore, we

[2]Since the annotation was done in a subjective manner, the annotated positions were not exactly the center positions of the vessels.

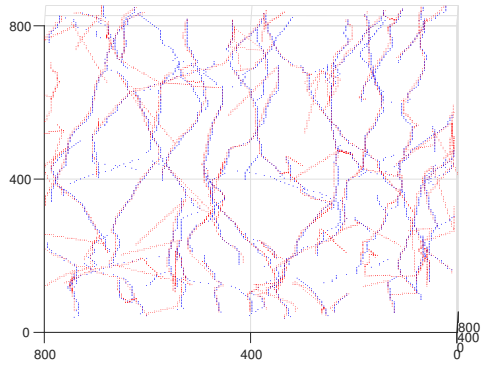

Figure 10. Comparison of the manual annotation and tracking results. Red dots indicate blood vessel curves obtained from the proposed method, and blue dots indicate those obtained from the manual annotation.

compared the center lines of tracking results and manual annotation. Figure 10 shows the center line of blood vessels. The results shows that most blood vessels were correctly tracked except vessel curves that run along the horizontal axis (x-y axis). Since our method tracks along a single axis, the method fails to track these vessel curves traversing the horizontal axis. In addition, some individual blood vessels were connected by the connecting step in our method and this cause false positives. The tasks to address these problems remain for future works.

In the quantitative evaluation, the method achieved that the recall is 0.873, the precision is 0.872 and the F-measure is 0.872. In addition, we also evaluated the accuracy of the bifurcation detection that is the number of correctly detected bifurcation points divided the number of the total detected bifurcation points. This proposed method achieved 0.741 for this metric. These results show the efficacy of the proposed method on such challenging data, where many capillaries are densely located and make dense networks.

5. Conclusion

We proposed a multi-object tracking based modeling method that first tracks multiple blood vessels in cross-sectional images along a single axis to make the vessel curves, and then connects them on the basis of the orientation of the vessel curves and intensities of original data. The approach, in which the method tracks vessels along only a single base-axis, is efficient comparing with current method that track individual vessels with searching the cross-sectional plane in each point. The results of experiments using a challenging real data-set demonstrate the efficacy of the proposed method, which are capable of modeling dense capillaries. To address the limitations of our method that hard to track vessels traversing along the vertical of base-axis, we will introduce three base-axes instead of using one axis in the future works.

Acknowledgments.

The authors would like to thank Dr. Shimano of National Institute of Informatics, Japan for useful discussion. The authors also applicate Mr. Yagi who is a program manager of ImPACT Program. This work was funded by ImPACT Program of Council for Science, Technology and Innovation (Cabinet Office, Government of Japan).

References

[1] R. Adams and L. Bischof. Seeded region growing. *IEEE Transactions on Pattern Analysis and Machine Intelligence*, 16(6):641–647, 1994.

[2] R. Bise, Y. Maeda, M. Kim, and M. Kino-oka. Cell tracking under high confluence conditions by candidate cell region detection-based association approach. *Proceeding of Biomedical Engineering*, 10.2316/P2013.791-057, 2013.

[3] C. Florin, N. Paragios, and J. Williams. Particle filters, a quasi-monte carlo solution for segmentation of coronaries. *Proceedings of MICCAI*, 3749:246–253, 2005.

[4] A. Frangi, W. Niessen, K. Vincken, and M. Viergever. Multiscale vessel enhancement filtering. *Proceedings of MICCAI*, pages 130–137, 1998.

[5] A. F. Frangi, W. J. Niessen, R. M. Hoogeveen, T. van Walsum, and M. A. Viergever. Quantitation of vessel morphology from 3d mra. *Proceedings of MICCAI*, 1679:358–367, 1999.

[6] O. Friman, M. Hindennach, C. Kuhnel, and H. Peitgen. Multiple hypothesis template tracking of small 3d vessel structures. *Medical Image Analysis*, 14:160–171, 2010.

[7] C. Kirbas and F. Quek. A review of vessel extraction techniques and algorithms. *ACM Computing Surveys*, 36(2):81–121, 2004.

[8] D. Lesage, E. Angelini, I. Bloch, and G. Funka-Lea. A review of 3d vessel lumen segmentation techniques: models, features and extraction schemes. *Medical Image Analysis*, 13(6):819–845, 2009.

[9] R. Manniesing, M. Viergever, and W. Niessen. Vessel enhancing diffusion: A scale space representation of vessel structures. *Medical Image Analysis*, 10(6):815–825, 2006.

[10] C. McIntosh and G. Hamarneh. Vessel crawlers: 3d physically-based deformable organisms for vasculature segmentation and analysis. *Proceedings of IEEE CVPR*, pages 1084–1091, 2006.

[11] B. Schmid, G. Shah, N. Scherf, M. Weber, K. Thierbach, C. Campos, I. Roeder, P. Aanstad, and J. Huisken. High-speed panoramic light sheet microscopy reveals global endodermal cell dynamics. *Nature Communications*, 3207, 2013.

[12] H. Shim, D. Kwon, I. Yun, and S. Lee. Robust segmentation of cerebral arterial segments by a sequential monte carlo method: particle filtering. *Comput. Methods and Programs in Biomedicine*, 84(2):135–145, 2006.

[13] K. Tainaka, S. Kubota, T. Suyama, E. Susaki, D. Perrin, M. Ukai-Tadenuma, H. Ukai, and H. Ueda. Whole-body imaging with single-cell resolution by tissue decolorization. *Cell*, 159:911–924, 2014.

[14] J. Tyrrell, E. Tomaso, D. Fuja, R. Tong, K. Kozak, R. Jain, and B. Roysam. Robust 3-d modeling of vasculature imagery using superellipsoids. *IEEE Transactions on Medical Imaging*, 26(2):223–237, 2007.

[15] A. Vasilevskiy and K. Siddiqi. Flux maximizing geometric flows. *IEEE TPAMI*, 24(12):1565–1578, 2002.

[16] S. Wan and W. Higgins. Symmetric region growing. *IEEE Transactions on Image Processing*, 12(9):1007–1015, 2003.

[17] O. Wink, W. Niessen, and M. Viergever. Fast delineation and visualization of vessels in 3d angiographic images. *IEEE Transactions on Medical Imaging*, 19(4):337–346, 2000.

[18] O. Wink, W. J. Niessen, and M. Viergever. Multiscale vessel tracking. *IEEE Transactions on Medical Imaging*, 23(1):130–133, 2004.